Check for updates

ADVANCED FUNCTIONAL MATERIALS
www.afm-journal.de

Microfluidic Platforms to Screen Granular Hydrogel Microenvironments for Tissue Regeneration

*Lisa A. Krattiger, Dilara Börte Emiroglu, Silvia Pravato, Lukas O. Moser, Olivia A. Bachmann, Simona Y. La Cioppa, Gabriel J. Rodriguez Rivera, Jason A. Burdick, Andrew J. deMello, Mark W. Tibbitt, and Martin Ehrbar**

Granular hydrogels have emerged as a promising class of biomaterials in medical research, enabling independent control of matrix stiffness within a porous biomaterial. Such microgel packings comprise interconnected pores and high surface-to-volume ratios. These features facilitate cell viability and nutrient diffusion, which are critical in enabling tissue regeneration. Despite the current interest in granular hydrogels for tissue engineering applications, only a few in vitro platforms are used to investigate cell interactions, limiting their design, and translation. In this study, microfluidic platforms able to reproducibly confine and immobilize microgels without the need for secondary cross-linking are developed. Protocols are established for the generation of human bone marrow-derived mesenchymal stem/stromal cells (hBM-MSC)-infiltrated microporous substrates and early-time responses of cells to their environment are studied. Further, a tissue invasion assay is established, where cells infiltrate granular materials at different rates depending on growth factor presence or material properties. This platform is compatible with a range of different granular materials, and it is envisioned to have significant utility as a pre-clinical tool for the rational design of materials for tissue healing applications.

1. Introduction

Biomimetic hydrogel materials with tuneable properties have received substantial attention for the delivery of cells and bioactive molecules for in vivo tissue regeneration. In recent years, the utility of interconnected micron-scale porosity in hydrogel biomaterials in eliciting tissue repair and regeneration has alleviated the need for rapid material degradation by delivered and/or infiltrating cells.[1] Such porous hydrogels can be formed via cryogelation, phase separation, the inclusion of leaching particles, or the assembly of micron-sized hydrogel building blocks (microgels) into granular hydrogels.[2–6] In particular, pioneering work by Segura and co-workers demonstrated the translational impact of granular hydrogels—or microporous annealed particle (MAP) gels—for minimally invasive injection into tissues, accelerating regeneration in murine skin wound models and stroke recovery.[7–9] In another study, granular hydrogels made from hyaluronic acid-based hydrogel particles induced an endogenous response in a chondral defect.[10] Moreover, Coronel et al. demonstrated the beneficial immunomodulatory effect of degrading granular hydrogels composed of poly(ethylene glycol) (PEG)-maleimide microgels.[11]

Owing to their particulate structure, granular hydrogels are highly versatile substrates for cell and biomolecule delivery.[12,13]

L. A. Krattiger, S. Pravato, L. O. Moser, O. A. Bachmann, S. Y. La Cioppa, M. Ehrbar
Department of Obstetrics
University Hospital Zurich
University of Zurich
Schmelzbergstrasse 12, Zurich 8091, Switzerland
E-mail: martin.ehrbar@usz.ch

The ORCID identification number(s) for the author(s) of this article can be found under https://doi.org/10.1002/adfm.202310507

© 2024 The Authors. Advanced Functional Materials published by Wiley-VCH GmbH. This is an open access article under the terms of the Creative Commons Attribution-NonCommercial-NoDerivs License, which permits use and distribution in any medium, provided the original work is properly cited, the use is non-commercial and no modifications or adaptations are made.

DOI: 10.1002/adfm.202310507

L. A. Krattiger, D. B. Emiroglu, O. A. Bachmann, S. Y. La Cioppa, M. W. Tibbitt
Macromolecular Engineering Laboratory
Department of Mechanical and Process Engineering
ETH Zurich, Sonneggstrasse 3, Zurich 8092, Switzerland
D. B. Emiroglu, A. J. deMello
deMello Laboratory
Department of Chemical and Bioengineering
ETH Zurich
Vladimir-Prelog-Weg, 1–5/10, Zurich 8093, Switzerland
G. J. R. Rivera, J. A. Burdick
Burdick Laboratory
BioFrontiers Institute and Department of Chemical and Biological Engineering
University of Colorado Boulder
596 UCB, Boulder, CO 80309, USA

They can be assembled with a wide range of compositions without compromising the viability of living cells.[14] Microfluidic templating is a commonly employed technique for generating spherical and uniform particles.[15–17] In addition, batch emulsification, fragmentation, mechanical sizing, and lithography can produce microgels of varying size and shapes.[16,18–22] Granular hydrogels are formed by assembling the microgel building blocks into jammed materials, which comprise user-defined and modular cellular microenvironments with diverse physical and biochemical properties. Despite the potential translational impact of granular hydrogels in tissue repair and regeneration, there are few studies that systematically investigate how microgel or granular hydrogel properties influence cell functions in a biologically relevant context. Anseth and co-workers have shown that human mesenchymal stromal cell (hMSC) clustering varies with scaffold pore size, leading to changes in their secretory profile.[23] In addition, particle shape induced differences in endothelial cell invasion and sprouting.[24] These studies provided insight into the mechanistic underpinnings of cell–material interactions within granular hydrogels yielding relatively simple design properties. However, to date, most in vitro evaluations rely on microparticle jamming and require secondary cross-linking for stabilization of the forming porous hydrogel. Accordingly, studies aimed at engineering sophisticated granular hydrogels and systematically investigating their ability to influence cell function and tissue regeneration are few and far between. For such studies to be conducted within granular materials in an efficient and high throughput manner, controlled assembly of the scaffold and minimal material use are desired. To this end, microfluidic in vitro culture platforms are attractive tools for studying complex cellular processes by enabling the formation of miniaturized 3D hydrogel scaffolds.[25–28] Importantly, microfluidic platforms allow real-time imaging of the sample as well as the controlled introduction of exogenous factors, such as cytokines and growth factors. In addition, the short nutrient flow distances observed in vivo can be mimicked via miniaturization of the culture environment.[29] Through the integration of microfluidic technologies and 3D hydrogel cultures, many fundamental processes, including tumor angiogenesis and intravasation, as well as the roles of matrix stiffness and interstitial flow in cell migration have been investigated.[30–32] Accordingly, we set out to combine the advantages of microfluidic cell culture platforms and granular hydrogels to engineer a platform able to screen granular hydrogels as robust and tunable cell microenvironments.

In this study, we present microfluidic platforms that can reproducibly confine and immobilize microgels with minimal material use. We establish protocols for the generation of human bone marrow-derived mesenchymal stromal cell (hBM-MSCs)-infiltrated granular hydrogels. We assess the early spreading, extracellular matrix (ECM) deposition, and migration of hBM-MSCs in the presence or absence of pro-migratory signals using confocal or real-time imaging. Moreover, we propose a novel tissue-healing model to assess infiltration of hBM-MSCs into the granular materials. We utilize this platform to observe cell infiltration over time as a method to determine adequate pro-migratory growth factor stimulation. Furthermore, we investigate the effect of microgel stiffness and cell infiltration and demonstrate the versatility of this platform to assess a range of different granular materials. Our results highlight the utility of the confinement platform for the investigation of a diverse range of cell–material interactions within granular materials.

2. Results

2.1. Microfluidic Platform for Spatial Confinement of Microgels

To investigate the interactions between hBM-MSCs and microgel-based granular biomaterials, we fabricated microfluidic devices via photolithography and soft lithographic techniques. The microfluidic platforms were designed to confine hBM-MSCs and microgels in a controlled fashion with minimal use of materials and cells (**Figure 1**). The simple confinement device consisted of a confinement chamber flanked by two media channels for medium exchange (**Figure 2a**). The confinement chamber was 1 mm wide, 4.6 mm long, and 175 µm high to allow for 3D packing of microgels. Separation between the confinement chamber and media channels was achieved with a pillar array with a spacing of 30 µm. This limited the escape of microgels while ensuring unobstructed medium flow. Microfluidic devices were sterilized by autoclaving and placed on 6-well plates for seeding and subsequent culture, which allowed minimal handling of individual devices and facilitated efficient imaging.

As a model granular system, we synthesized microgels of controlled size and stiffness according to published methods.[33] Briefly, poly(ethylene glycol) (PEG) macromers end-functionalized with norbornene (PEGNB) were mixed with di-thiol linker (dithiothreitol; DTT), photoinitiator (lithium phenyl-2,4,6-trimethylbenzoylphosphinate; LAP), and the cell adhesion motif CRGDS. Droplets of the polymer mixture were generated using microfluidic flow focusing devices, where streams of hydrogel precursor solution and oil supplemented with surfactants were delivered at defined flow rates. The collected droplets were then cross-linked with light (λ = 365 nm; I = 15 mW cm^{-2}; t = 60 s) and washed thoroughly to remove residual oil. To produce granular hydrogels as porous microenvironments, a suspension of microgels was prepared in a solution of PBS containing a final concentration of 0.4% methylcellulose that increased the viscosity of the suspending medium to create a homogeneous dispersion and prevented sedimentation of microgels. We then seeded microgels into the microfluidic devices by injecting 40 µL of the suspension into the confinement chamber until it was filled (Figure 2b). The interconnected void space was visualized by perfusing the device with FITC-Dextran (500 kDa) (Figure 2b inset).

2.2. hBM-MSC Behavior On-Chip after Co-Confinement

Dilute suspensions of PEGNB microgels (network modulus of 38 kPa) and Hoechst-labeled hBM-MSCs at different concentrations (low, intermediate, and high; corresponding to 2.2, 6.6, and 19.8 × 10^6 cells mL^{-1}, respectively) were co-confined in the microfluidic chamber (Figure 2c). Microgels remained within the chamber, while excess fluid along with some of the loaded cells escaped between the pillars. Shortly after seeding, devices were imaged and the number of hBM-MSCs present within the confinement chamber was quantified by counting Hoechst-stained

© 2024 The Authors. Advanced Functional Materials published by Wiley-VCH GmbH

16163028, 0, Downloaded from https://onlinelibrary.wiley.com/doi/10.1002/adfm.202310507 by ETH Zurich, Wiley Online Library on [21/05/2024]. See the Terms and Conditions (https://onlinelibrary.wiley.com/terms-and-conditions) on Wiley Online Library for rules of use; OA articles are governed by the applicable Creative Commons License

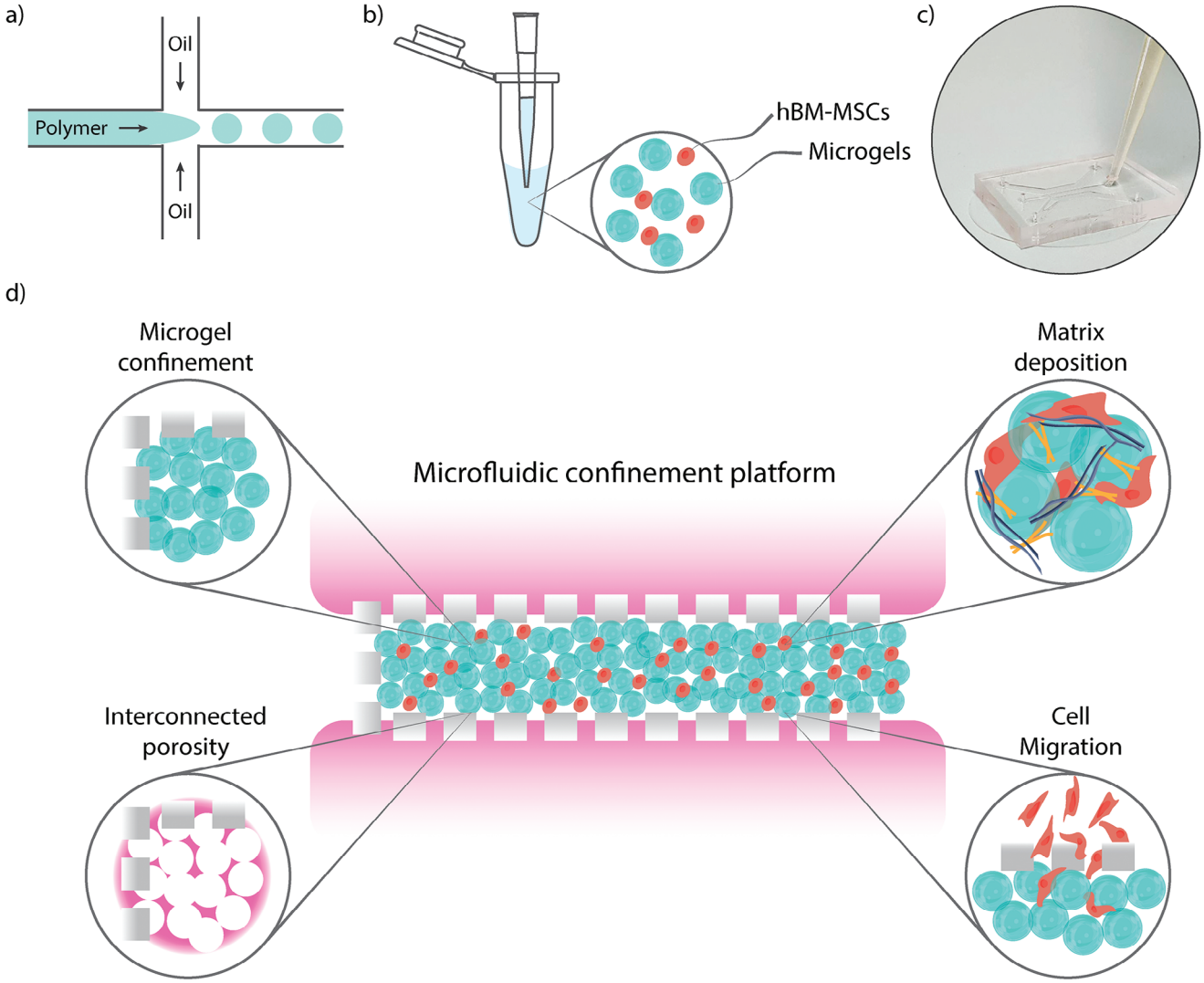

Figure 1. Microfluidic confinement device for the controlled generation of granular materials to study cell behavior. a) Granular material building blocks used throughout the study (unless stated otherwise) were generated by microfluidic droplet formation of PEGNB precursors yielding uniform, spherical microgels. b) For direct co-confinement, dilute suspensions of microgels and human bone marrow-derived mesenchymal stromal cells (hBM-MSCs) were prepared immediately prior to seeding. c) Suspensions were injected with a standard micropipette into the confinement chamber until the chamber was filled. d) Using this platform, microgels were successfully confined within the device, creating a substrate characterized by an interconnected, void space. This microporous substrate readily allowed hBM-MSCs to deposit their own ECM and to colonize the granular material and migrate between the pores.

nuclei. The initial cell concentration in the seeding suspension controlled the number of cells in the chip. With low concentration cell suspensions, 1050 ± 250 cells were captured within the confinement chamber, while for the intermediate and high concentrations 2420 ± 170 and 4690 ± 450 cells were captured, respectively (Figure 2d). hBM-MSCs spread around the microgels as early as 3 h after seeding (Figure 2e). After 3 days in culture, hBM-MSCs had established interconnected cell networks within the 3D void spaces of the granular biomaterial (Figure 2e,f). These networks were rich in extracellular matrix, as exemplified by immunostaining for fibronectin and collagen I (Figure 2g). The projected area of the signals for F-actin and ECM molecules, which served as a readout parameter for cell spreading and matrix deposition, were also quantified (Figure 2h). Fibronectin and collagen I covered a comparably large area, which was, however significantly smaller than for F-actin. In addition to cell spreading and ECM deposition, the culture format enabled quantification of cell migration. To monitor hBM-MSC migration, cells were labeled with Hoechst DNA-dye prior to seeding. Due to their controlled co-confinement, single nuclei could be tracked during time-lapse studies that started shortly after seeding (Figure 2i). Images were acquired over 14 h at intervals of 5 min. Cells migrated freely within the void spaces of the granular hydrogel (Figure 2j; Supporting Video S1, Supporting Information). The addition of 100 ng mL^{-1} PDGF-BB did not appear to impact the total distance of cell migration over 14 h (87 +/−41 µm with PDGF-BB as compared with 73 +/−38 µm in the absence of PDGF-BB). As a complement to studies with single cells, hBM-MSC spheroids (200

© 2024 The Authors. Advanced Functional Materials published by Wiley-VCH GmbH

16163028, 0, Downloaded from https://onlinelibrary.wiley.com/doi/10.1002/adfm.202310507 by ETH Zurich, Wiley Online Library on [21/05/2024]. See the Terms and Conditions (https://onlinelibrary.wiley.com/terms-and-conditions) on Wiley Online Library for rules of use; OA articles are governed by the applicable Creative Commons License

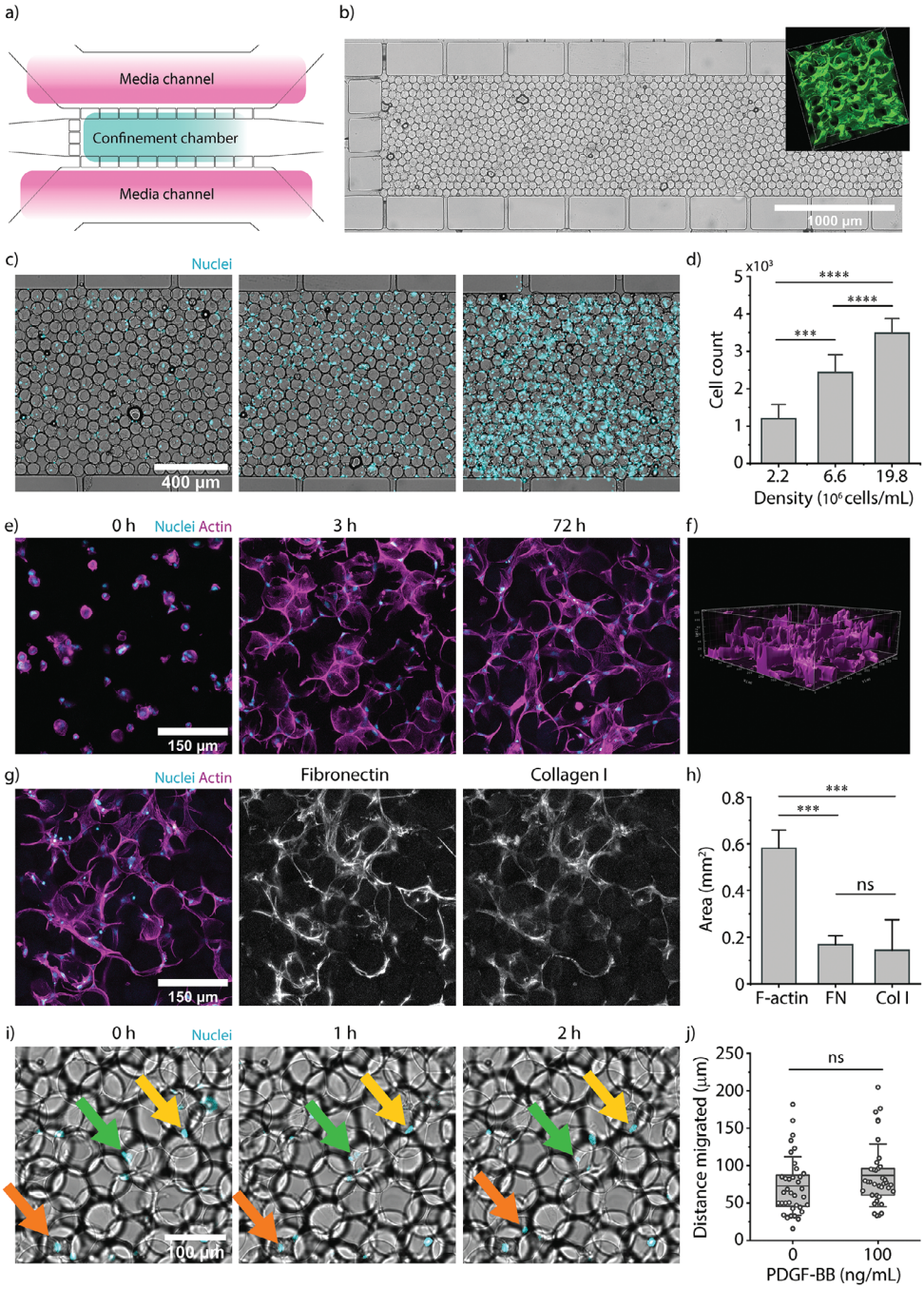

Figure 2. On-chip microgel co-confinement with hBM-MSCs. a) Schematic of a device featuring two media channels for medium perfusion and a central chamber for microgel (and cell) confinement (confinement chamber). Width of the central chamber is 1 mm; 490 µm long pillars are spaced 30 µm apart. b) Bright-field image of 75 µm diameter PEGNB-microgels confined on the chip. Inlet showing reconstructed void space in between microgels visualized by perfusing 500 kDa FITC-Dextran and acquiring confocal stacks (z-step 2.41 µm; total height 90 µm). c) Overlays of bright-field and Hoechst signal of Hoechst-stained hBM-MSCs co-confined on the chip at different initial seeding densities (2.2, 6.6, and 19.8 × 10^6 cells mL^{-1}, from left to right, respectively). d) Quantification of nuclei based on Hoechst staining within the central chamber immediately after seeding; ANOVA with Holm-Šídák correction; $n = 4$. e) Maximum intensity projection of confocal stacks (z-step 2.41 µm, total height 100 µm) of samples fixed immediately, after 3 h or after 72 h and stained for F-actin (magenta) and nuclei (DAPI; cyan). f) 3D reconstruction of hBM-MSCs after 72 h generated from a confocal stack (z-step 0.5 µm; total height 125.5 µm). g) Maximum intensity projection of confocal stacks (z-step 2.41 µm, total height 100 µm) of samples fixed after 72 h and stained for F-actin (magenta), nuclei (DAPI; cyan), fibronectin (gray, middle) and collagen I (gray, right). h) Quantification of F-actin- fibronectin- and collagen I-positive area within the confinement chamber after 72 h of culture; ANOVA with Holm-Šídák correction; $n = 4$. i) Time lapse image series of bright-field and Hoechst signals at 0, 1, and 2 h. Ten percent of hBM-MSCs were Hoechst-labeled prior to seeding and arrows indicate individual stained nuclei that can be tracked over time. j) Quantification of total migrated distance over 14 h; $n = 36$ (0 ng mL^{-1} PDGF-BB) and $n = 37$ (100 ng mL^{-1} PDGF-BB) tracks measured from two culture chambers; Mann–Whitney test. Data in bar plots are represented as mean +/- SD. $^{***}p < 0.001$, $^{****}p < 0.0001$, ns not significant.

© 2024 The Authors. Advanced Functional Materials published by Wiley-VCH GmbH

16163028, 0, Downloaded from https://onlinelibrary.wiley.com/doi/10.1002/adfm.202310507 by ETH Zurich, Wiley Online Library on [21/05/2024]. See the Terms and Conditions (https://onlinelibrary.wiley.com/terms-and-conditions) on Wiley Online Library for rules of use; OA articles are governed by the applicable Creative Commons License

cells/spheroid) were co-confined with the microgels, demonstrating outgrowth into the material in response to PDGF-BB (Figure S1, Supporting Information).

2.3. Double-Compartment Platform to Assess Cell Infiltration into Granular Materials

The ability of an implanted biomaterial to support cell migration and infiltration is crucial for tissue integration and growth. In fact, granular biomaterials are often designed with the express goal of facilitating cell infiltration into the applied biomaterial for local tissue repair. Therefore, we developed a multi-chamber microfluidic platform to model the interface of host tissue and the granular healing material.

More specifically, we designed a modified microfluidic device featuring a "tissue" chamber adjacent to the confinement chamber (**Figure 3**a,b). In this device, a tissue mimic was formed in the tissue chamber, allowing for the tracking and quantification of transmigration of cells into the confinement chamber. For enhanced transmigration and nutrient exchange, pillars surrounding the tissue chamber were spaced 80 µm apart. In contrast, to prevent microgel escape between the pillars facing the outlet and the lower media channel (the sides not obstructed by the pre-cast tissue mimic), the pillars were spaced 60 µm apart. The triangular shape was chosen to maximize the interface of the two channels, as the narrow and long gap between pillars in the single-chamber design did not appear to allow for facile transmigration (Figure S2, Supporting Information). The matrix for the tissue mimic consisted of hBM-MSCs encapsulated in a soft hydrogel made from transglutaminase-cross-linked PEG at 1.7 wt% (0.4 kPa) (Figure S3, Supporting Information), featuring an RGD adhesion motif and an MMP-cleavable sequence combined with collagen I at 0.25 µg mL^{-1}. This material polymerized 3 min after the addition of the cross-linking enzyme FXIIIa, which allowed for injection into the tissue chamber of six devices per hydrogel batch. After polymerization, the confinement chamber and media channels were flushed with basal culture medium and allowed to equilibrate at 37 °C for 30 min. Next, the confinement chamber was filled with microgels, as described above, but without the addition of cells (Figure 3b). Microgels were functionalized with RGD adhesion motifs to facilitate cell attachment. In the absence of these adhesive sites, cell migration was strongly reduced (Figure S4, Supporting Information). The ability of the cells to migrate into the confinement chamber was observed over a period of seven days. To monitor this invasion longitudinally, Hoechst-labeled hBM-MSCs were encapsulated in the tissue chamber and interface regions were imaged daily (Figure S5, Supporting Information). The first cells began to invade between days 1 and 3 and continued to invade the microgel compartment until day 7.

To assess the suitability of our platform to quantitatively screen for differences in infiltration-potential, a proof-of-concept evaluation based on the titration of pro-migratory PDGF-BB was conducted. Devices featuring both tissue and confinement chambers were seeded as described above using PEGNB microgels. After filling the confinement chamber, basal culture medium with (25 and 100 ng mL^{-1}) or without PDGF-BB was added to the devices. After 3 days in culture, the samples were fixed and stained for nuclei, F-actin, and fibronectin (Figure 3c). The invasion distance was determined by the position of the individual nuclei per condition across the width of the confinement chamber. While many cells localized near the interface for all conditions, more nuclei were detected at the far end of the chamber in the presence of PDGF-BB (Figure 3c). In all conditions, the transmigrated cells spread around the microgels in a similar manner to cells that were directly co-confined (Figure 3d). They also deposited fibronectin. Image-based quantification of the average number of nuclei within the confinement chamber after 3 days of culture suggests a positive correlation between the number of transmigrated cells and PDGF-BB concentration (Figure 3e). The same trend was observed for the area of F-actin-positive signal; however, the differences were not statistically significant (Figure 3g). Further, fibronectin deposition was significantly increased in the presence of PDGF-BB at both concentrations when compared with basal medium (Figure 3h).

2.4. Microgel Stiffness Influences the Invasion of hBM-MSCs in Microfluidic Tissue Healing Model

To investigate the impact of material stiffness on cellular response, we produced PEGNB microgels with polymer network moduli of 1.3, 7, and 38 kPa, respectively (Figure S6, Supporting Information). As expected, the granular scaffold modulus increased as a function of the network modulus (**Figure 4**a). The three types of microgels exhibited a comparable size distribution, with the 5% and 10% PEGNB microgels measuring ≈70 µm, and the 3.5% microgels slightly larger at 75 µm (Figure S7, Supporting Information). When filling the confinement chamber with a pillar gap of 60 µm, we successfully confined microgels of 7 and 38 kPa, while the softer microgels (1.3 kPa) squeezed through the pillars due to their high deformability. By reducing the pillar gap to 40 µm, we were also able to confine softer microgels (1.3 kPa) (Figure S8, Supporting Information). The total exchange area was kept constant between the two device designs. After confinement, we assessed the porosity of the constructs (Figure 4b), pore diameter distribution (Figure 4c), and average pore diameters (Figure 4d) by perfusing FITC-dextran (500 kDa MW) through the side channels. The 38 kPa microgels exhibited the highest porosity (46%), with an average pore size of 36 µm. The chamber containing 7 and 1.3 kPa PEGNB microgels featured less porosity (37% and 34%) and average pore size of 19 and 23 µm, respectively. Observed porosities were within the range of reported values for granular materials produced by other methods.[10,34]

Samples with hBM-MSCs in the tissue-mimicking compartment were cultured in the presence of 25 ng mL^{-1} PDGF-BB for 72 h before being fixed and stained for nuclei, F-actin, and Ki-67 (Figure 4e). hBM-MSCs efficiently spread on the surface of the microgels, and Ki-67-positive cells were detected in all samples (Figure 4f), indicating effective cell adhesion and proliferation.

The distance traveled by the hBM-MSCs from the interface region was analyzed to investigate how microgel stiffness affected cell migration. Images taken on fixed samples were utilized to determine the locations of the nuclei. Cells exhibited longer migration distances in the presence of 38 kPa PEGNB microgels, while shorter distances were observed for softer hydrogels (Figure 4g). The total number of cells that had migrated into the confinement

© 2024 The Authors. Advanced Functional Materials published by Wiley-VCH GmbH

16163028, 0, Downloaded from https://onlinelibrary.wiley.com/doi/10.1002/adfm.202310507 by ETH Zurich, Wiley Online Library on [21/05/2024]. See the Terms and Conditions (https://onlinelibrary.wiley.com/terms-and-conditions) on Wiley Online Library for rules of use; OA articles are governed by the applicable Creative Commons License

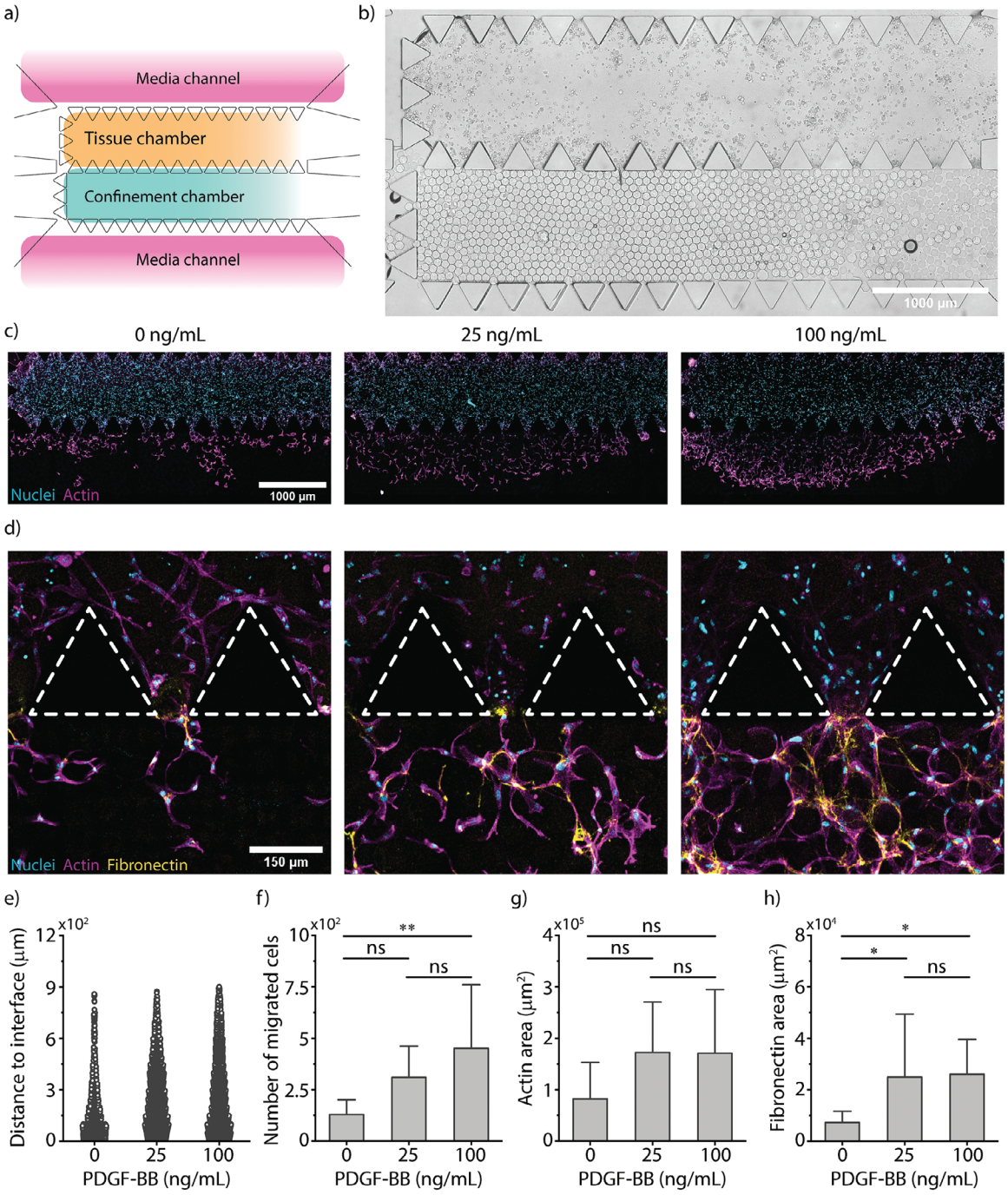

Figure 3. Multi-chamber microfluidic platform to study hBM-MSC infiltration in response to growth factor stimulation. a) Schematic of the two-chamber device featuring a tissue chamber adjacent to the confinement chamber flanked by media channels for medium perfusion. The width of the tissue chamber is 800 µm and triangular pillars with a side length of 250 µm which are spaced 80 µm apart to facilitate cell transmigration. The width of the confinement chamber is 1 mm and the triangular pillars separating the chamber toward the outlet and the bottom media channel are spaced 60 µm apart to limit microgel escape. b) Bright-field overview image of the two-chamber device acquired on the day of seeding. c) Maximum intensity projections of confocal stacks showing both the tissue and the confinement chambers (z-step 10 µm, total height 100 µm) of samples fixed after 72 h and stained for F-actin (magenta), nuclei (DAPI; cyan) and fibronectin (not shown). Samples were cultured with different concentrations of PDGF-BB (0, 25 and 100 ng mL^{-1} from left to right). d) Interface regions corresponding to overviews shown in (c), also showing fibronectin (yellow). e) Image-based quantification of the distance of single nuclei detected in the confinement chamber from the interface between the two chambers. A total of 1429, 3097, and 5434 nuclei were analyzed from $n \geq 10$ devices per condition. f) Quantification of absolute number of nuclei detected within the confinement chamber after 72 h of culture; ANOVA with Holm-Šídák correction; $n \geq 10$. g) Quantification of F-actin- and fibronectin-positive area within the confinement chamber after 72 h of culture; Kruskal–Wallis with Dunn's test; $n \geq 10$. h) Quantification of fibronectin-positive area; ANOVA with Holm-Šídák correction; $n \geq 10$. Data in bar plots are represented as mean +/−SD. $^{*}p < 0.05$, $^{**}p < 0.01$, ns not significant.

© 2024 The Authors. Advanced Functional Materials published by Wiley-VCH GmbH

16163028, 0, Downloaded from https://onlinelibrary.wiley.com/doi/10.1002/adfm.202310507 by ETH Zurich, Wiley Online Library on [21/05/2024]. See the Terms and Conditions (https://onlinelibrary.wiley.com/terms-and-conditions) on Wiley Online Library for rules of use; OA articles are governed by the applicable Creative Commons License

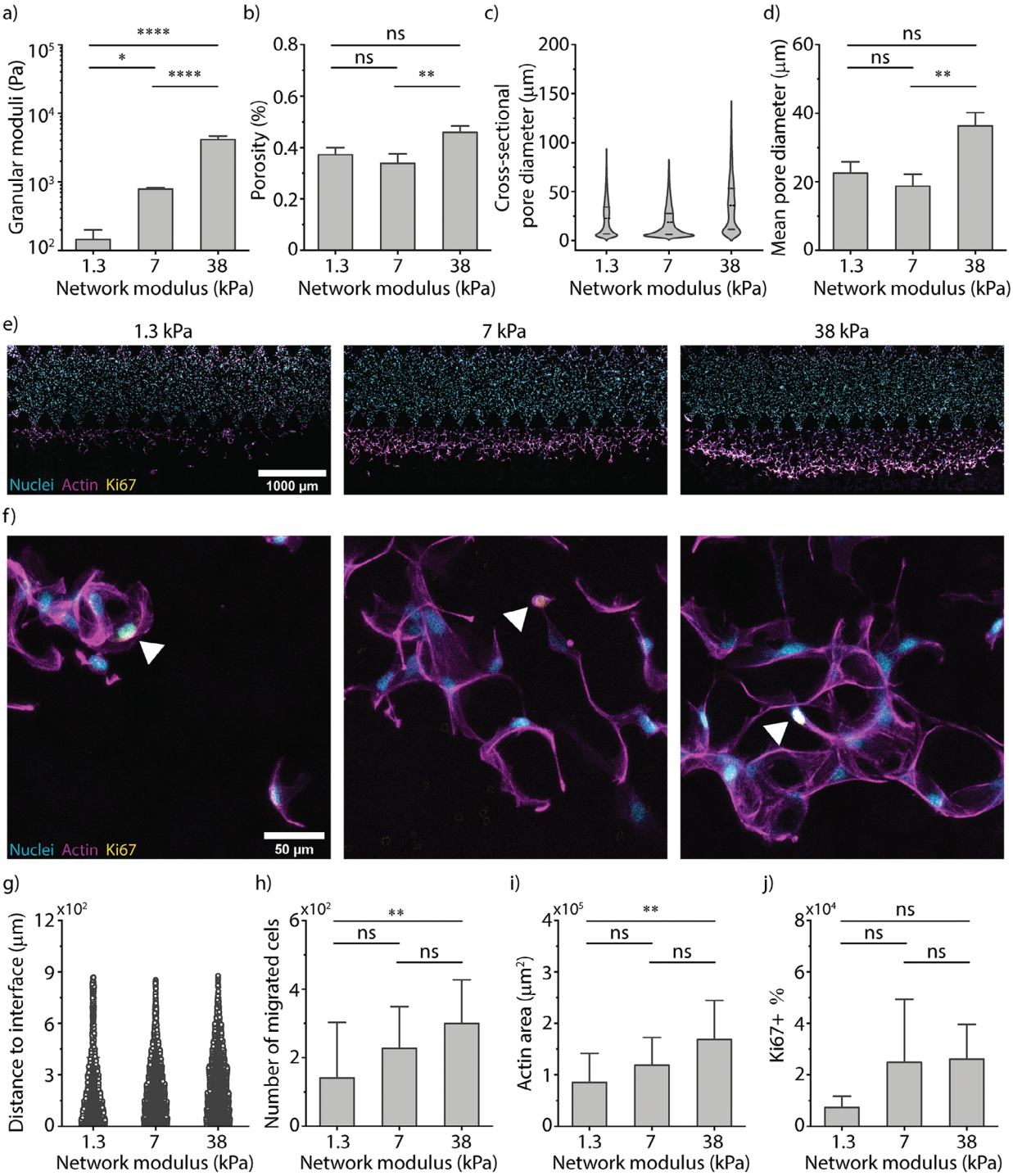

Figure 4. Impact of material stiffness on scaffold properties and cellular response. a) Representation of the granular shear moduli for 1.3 kPa (3.5%, left), 7 kPa (5%, middle), and 38 kPa (10%, right) PEGNB microgels; ANOVA with Holm-Šídák correction; $n = 3$. b) Quantification of the porosity within the confinement chamber for microgels of the different stiffnesses; Kruskal–Wallis with Dunn's test; $n = 5$. c) Quantification of pore size distribution and d) inter-microgel pore diameter; Kruskal–Wallis with Dunn's test; $n = 5$. e) Maximum intensity projections of confocal stacks showing tissue and confinement chambers (z-step: 10 µm, total height: 90 µm) with the different PEGNB microgels, cultured with PDGF-BB (25 ng/mL). Samples were fixed after 72 h and stained for F-actin (magenta), nuclei (DAPI; cyan) and Ki-67 (yellow). f) Regions corresponding to samples shown in overviews in (e), highlighting Ki-67 (yellow) with arrows. g) Quantification of the distance of individual nuclei detected in the confinement chamber from the interface between the two chambers using image analysis: $n \geq 12$ devices per condition. h) Quantification of absolute number of nuclei detected within the confinement chamber after 72 h of culture in the three different confinement chambers; Kruskal–Wallis with Dunn's test; $n \geq 12$. i) Quantification of F-actin-positive area within the confinement chamber after 72 h of culture; $n \geq 12$ devices per condition. j) Quantification of percentage of Ki-67-positive nuclei; ANOVA with Holm-Šídák correction; $n = 5$. Data in bar plots represented as mean +/−SD. $^{*}p < 0.05$, $^{**}p < 0.01$, $^{****}p < 0.0001$, ns not significant.

© 2024 The Authors. Advanced Functional Materials published by Wiley-VCH GmbH

16163028, 0, Downloaded from https://onlinelibrary.wiley.com/doi/10.1002/adfm.202310507 by ETH Zurich, Wiley Online Library on [21/05/2024]. See the Terms and Conditions (https://onlinelibrary.wiley.com/terms-and-conditions) on Wiley Online Library for rules of use; OA articles are governed by the applicable Creative Commons License

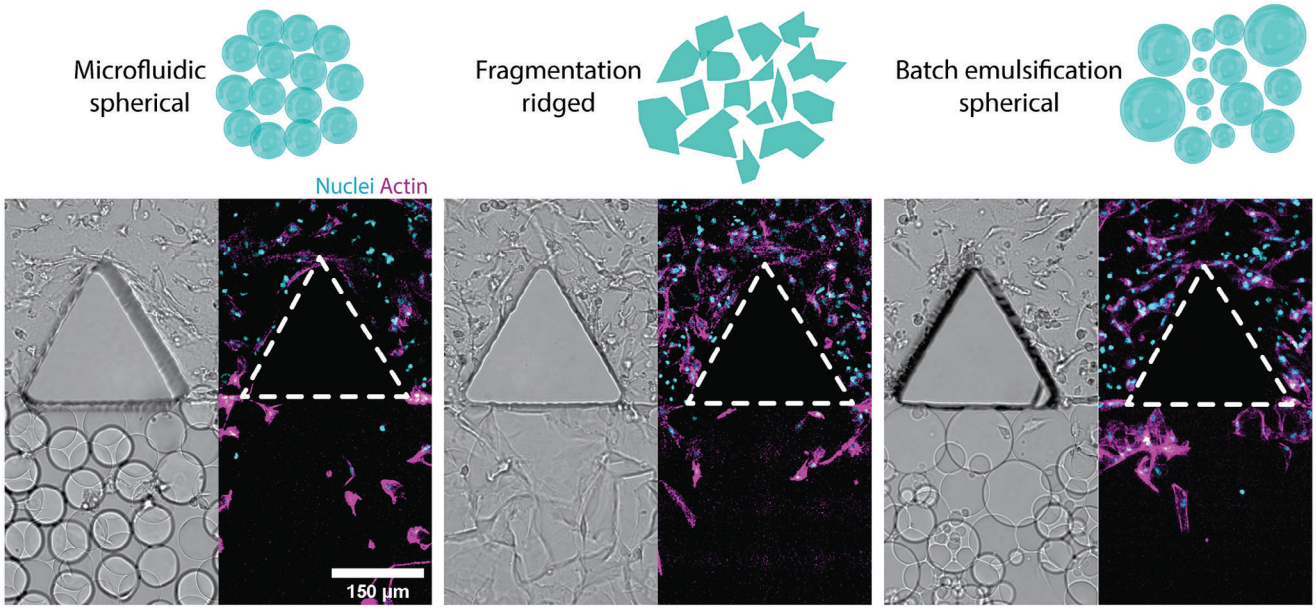

Figure 5. Cell invasion into compartments with diverse granular materials. Different types of granular materials can be loaded within the confinement chamber. Left side of images: Bright-field day 7-images of interface regions for devices testing PEGNB-based microgels generated via microfluidic droplet formation, NorHA-based microgels generated via extrusion fragmentation, and GelMA-based microgels generated via batch emulsification; right side of images: corresponding maximum intensity projections showing F-actin and nuclei.

chamber by the end of culture increased with the stiffness of the microgels (Figure 4h), as did the area of F-actin-positive signal (Figure 4i). However, no significant differences in the percentage of Ki-67-positive nuclei or nuclear to cytoplasmic ratio of YAP were observed between the conditions (Figure 4J; Figure S9, Supporting Information).

2.5. Healing Model for the Probing of Diverse Granular Materials

To demonstrate the versatility of this platform to assess the healing potential of various granular hydrogels through infiltration of tissue-resident cells, we filled the confinement chamber with microgels generated using different techniques and based on distinct precursor materials. In addition to the PEGNB microgels (network shear modulus 38 kPa) produced by droplet-based microfluidics, we used norbornene-functionalized hyaluronic acid (NorHA)-based microgels (network shear modulus 20 kPa) generated by fragmentation of a bulk gel[21] and methacrylated gelatin (GelMA)-based microgels (network shear modulus 8 kPa) generated by batch emulsion. The fragmentation-based NorHA microgels and the batch emulsion-based GelMA microgels were also successfully confined on the chip (**Figure 5**). Spontaneous cellular invasion from the tissue chamber into the confinement chamber was observed for all materials tested as visualized by staining for nuclei and F-actin after 7 days of culture in basal medium.

3. Discussion

Granular hydrogels featuring physiologically relevant pore sizes (on the order of tens of µm) and injectability demonstrate broad potential as regenerative biomaterials. While their use has increased substantially in recent years, few granular biomaterials have been specifically tailored for the intended use case. Therefore, platforms to screen a wide range of granular biomaterials and study cell behavior or ingrowth of cells from a neighboring tissue may help engineer suitable granular materials for different applications. In this work, we developed user-friendly microfluidic platforms that enable the in vitro characterization and optimization of granular hydrogels as cell culture and tissue regeneration substrates. Current methods to assemble the building blocks into granular scaffolds consist of centrifugation or vacuum filtration and generated constructs are usually relatively large (≈100 µL).[24,35] In addition, secondary cross-linking is often necessary to maintain their shape for in vitro cell-based assays.[36,37] Notably, our microfluidic platforms allowed the stable confinement of low volumes (2–5 µL) of PEGNB microgels with different levels of stiffness (network stiffness between 1.3 and 38 kPa) to form homogeneous granular hydrogel constructs. These constructs had interconnected pores and a porosity comparable to that of centrifugation-jammed microgels of the same type.[38] The pillar spacing (30 µm) used in our microfluidic device allowed for the co-confinement of ≈75 µm diameter microgels and viable cells. Using this relatively simple approach, some cells are lost during the co-confinement, potentially restricting their use for the testing of rare cell populations in this specific setup. Nonetheless, cells were homogeneously distributed throughout the construct and their density could be tuned by adjusting their number during the confinement. In addition, longitudinal imaging of the constructs was possible owing to the stable on-chip confinement. Importantly, we observed fast spreading (3 h post seeding) of hBM-MSCs on the surface of the microgels and the deposition of canonical tissue healing-associated ECM

© 2024 The Authors. Advanced Functional Materials published by Wiley-VCH GmbH

16163028, 0, Downloaded from https://onlinelibrary.wiley.com/doi/10.1002/adfm.202310507 by ETH Zurich, Wiley Online Library on [21/05/2024]. See the Terms and Conditions (https://onlinelibrary.wiley.com/terms-and-conditions) on Wiley Online Library for rules of use; OA articles are governed by the applicable Creative Commons License

proteins, fibronectin, and collagen I[39] after 3 days of culture. Interestingly, under standard culture conditions co-confined hBM-MSCs actively migrated through the pores of the granular hydrogels; the migration rates did not significantly increase upon stimulation with PDGF-BB, a known activator of cell migration. These in vitro observations reinforce the idea that granular constructs are often inherently conducive for healing-relevant functions of cells, including migration and matrix deposition. Systematic investigation of the effect of regeneration-relevant factors with such platforms may enable improved prediction of their in vivo functionality.

When used for tissue regeneration, biomaterials are brought in close contact with the defective tissue, where they ideally promote the invasion and differentiation of host cells.[40] Therefore, to mimic the high density of host cells typically present at the biomaterial interface, we co-confined spheroids generated from 200 hBM-MSCs (≈100 µm in diameter) and microgels in our microfluidic platform. In this setting, the addition of PDGF-BB significantly increased the outgrowth of cells from the original cluster into the pores of the granular system. While this finding is in line with earlier observations in nanoporous hydrogels,[41] the outgrowth of cells might not adequately represent the ingrowth into biomaterials and the use of cell spheroids does not adequately represent structured tissues.

To model the interface of the host tissue and the implanted granular hydrogels more closely, we adapted our microfluidic device such that the granular hydrogel could be confined adjacent to an engineered tissue mimic. As expected, hBM-MSCs only migrated across the interface when there was a granular material in close contact with the bulk hydrogel in the tissue compartment. The invasion was also sensitive to the presence of suitable cell adhesion sites, as shown by the lack of migrating cells in the absence of RGD (Figure S5, Supporting Information). In addition, hBM-MSCs invaded the granular materials more efficiently (higher number of invading cells and larger distances) with increased concentrations (25 and 100 ng mL^{-1}) of a pro-migratory stimulus, PDGF-BB. During this invasion, hBM-MSCs also deposited fibronectin, especially in the presence of PDGF-BB. For the higher dose of PDGF-BB, the architecture of the final cell- and ECM-networks strongly resembled those of directly co-confined hBM-MSCs. Finally, hBM-MSCs migration was influenced by the use of granular hydrogels composed of microgels with different stiffness. These findings demonstrate how this novel invasion platform can be used to systematically study cellular infiltration into granular materials while simultaneously assessing effects of stiffness and interactions of healing-relevant soluble factors. This ability to evaluate both individual and several parameters at a time will be important since the variation of one material parameter can influence multiple granular hydrogel characteristics.

To demonstrate that this microfluidic platform can be applied to assay a broad spectrum of microgels, we used different base materials and different fabrication techniques, namely NorHA microgels (network shear modulus 20 kPa) made by fragmentation and GelMA microgels (network shear modulus 8 kPa) generated through batch emulsification, in addition to the PEG-based microgels (network shear modulus 38 kPa) produced via microfluidic templating.[21,42] hBM-MSCs invaded each of the granular hydrogels over time, even in the absence of PDGF-BB. While our microfluidic platform worked reproducibly with stiffer and homogeneously sized (≈75 µm) PEGNB and (≈100 µm) NorHA microgels, the wide size range and low stiffness of GelMA microgels produced by batch emulsification (≈10–150 µm) proved more challenging. Small microgels easily escaped between the pillars and larger ones obstructed the injection. We show that by adapting the pillar gap size, the platform can be tuned to accommodate further microgel designs. While the presented data rely mostly on homogeneous granular hydrogel formulations, our platforms are suitable for the investigation of hydrogels composed of various building blocks.

Biomaterials-supported tissue healing is a complex process that relies on multiple functions, including the recruitment of immune and tissue progenitor cells, proliferation and differentiation of recruited progenitor cells, and remodeling of the applied biomaterial.[43] We previously observed in in vivo studies that among the factors that largely affect nanoporous biomaterial-guided bone regeneration is the efficiency of host cell infiltration.[44] The presented microfluidic platforms here enable the assessment of hBM-MSC infiltration, proliferation, and ECM deposition in granular hydrogel formulations under defined in vitro conditions. This highlights its utility for the animal-free selection and optimization of granular hydrogel formulations with promising healing properties before their thorough in vivo testing. Future studies will apply similar protocols to investigate the role of vascular, immune, or other healing-relevant cell types in various tissue regeneration applications.

Taken together, we envision these models to be of use in the optimization of filler granular implantable materials to bridge skin, bone, or other tissue defects. In the first stage, a new type of granular material, surface modification, or growth factor supplementation could be tested by directly co-confining cells or cell clusters with the material. If the desired behavior is observed, cell invasion into the granular material can be assessed using the two-chamber device. Owing to the low volumes of material required and facile application of the devices, experiments can be performed on a reasonably large scale. We believe that these platforms can serve as useful pre-clinical screening tools to optimize healing conditions before in vivo testing is performed.

4. Conclusion

In this work, we designed a microfluidic cell culture platform that systematically confines microgels to generate porous, granular hydrogel microenvironments. We reproducibly co-confined hBM-MSCs along with microgels and assessed their number, spreading, extracellular matrix deposition, as well as migration via immunofluorescence, time-lapse imaging, and image-based quantification. The initial cell suspension concentration controlled the cell number within the chamber. After 3 days of co-confinement, hBM-MSCs readily deposited ECM components fibronectin and collagen I and migrated within the 3D porous environment. We investigated the ingrowth of cells into the created porous environments by designing an adjacent tissue chamber, filled with an hBM-MSC-containing, enzymatically cross-linked PEG hydrogel. We showed that a fraction of the hBM-MSCs encapsulated in a bulk hydrogel transmigrated from the tissue chamber and colonized the confined microgels in the neighboring confinement chamber in a novel proposed tissue healing model. Transmigration was stimulated in this model

© 2024 The Authors. Advanced Functional Materials published by Wiley-VCH GmbH

16163028, 0, Downloaded from https://onlinelibrary.wiley.com/doi/10.1002/adfm.202310507 by ETH Zurich, Wiley Online Library on [21/05/2024]. See the Terms and Conditions (https://onlinelibrary.wiley.com/terms-and-conditions) on Wiley Online Library for rules of use; OA articles are governed by the applicable Creative Commons License

by the addition of PDGF-BB, was dependent on the presence of adhesion sites on the microgels and varied with microgel stiffness. Furthermore, the applicability of the platform to probe a range of different granular materials was tested. We envision this system to be a versatile and modular platform to investigate a wide variety cell-granular material interactions which can be key in imparting regenerative response in vivo.

5. Experimental Section

Methods—Synthesis of 8-Arm PEGNB: The synthesis of 8-arm PEG-norbornene (PEGNB) was done as described previously.[45] Briefly, 8-arm PEG-NH_2HCl (M_n = 10 000 g mol^{-1}; 8 g, 0.8 mmol PEG, 6.4 mmol NH_2, JenKem Technology USA) was dissolved in anhydrous dimethylformamide (DMF; 5 mL). First, *N,N*-Diisopropylethylamine (DIPEA; 4.46 mL, 25.6 mmol, 4 eq.) and 1-[bis(dimethylamino)methylene]−1H-1,2,3-triazolo[4,5-b]pyridinium 3-oxide hexafluorophosphate] (HATU; 4.86 g, 12.8 mmol, 2 eq.) were added to the PEG solution. Next, 5-norbornene-2-carboxylic acid; (3.12 mL, 25.6 mmol, 4 eq.) was added to the mixture before stirring overnight at room temperature (RT). The reaction mixture was precipitated twice in diethyl ether at 4 °C and the precipitate dialyzed in a regenerated cellulose dialysis membrane (1 kDa MWCO, Spectrum Labs) membrane against dH_2O for 3 days. Finally, the aqueous polymer solution was frozen and lyophilized.

Synthesis of 8-arm TG-PEG: Hydrogel precursors were synthesized as previously described.[46,47] Briefly, 8-arm PEG-VS (PEG-vinylsulfone, 40 kDa) was functionalized with peptides containing a cysteine cassette described previously (ERCG), which was optimized for its reaction with PEG-VS. Next, factor XIII (FXIII) glutamine acceptor substrate sequence (Gln; H-NQEVSPL-ERCG-NH_2; Bachem) or a matrix metalloproteinase degradable lysine donor substrate (MMP sensitive-Lys; Ac-FKGG-GPQGIWGQ-ERCG-NH_2) at a 1.2 molar excess of peptides over PG-VS was reacted in triethanolamine (Sigma) for 2 h at 37 °C and at pH 8.0. The 8-arm PEG-Gln and 8-arm PEG-MMP sensitive-Lys precursors were subsequently dialyzed against pure water before being lyophilized and stored at −20 °C. For activation of the cross-linking enzyme (FXIIIa), transglutaminase FXIII (200 U mL^{-1}, Fibrogammin P; CSL Behring), was incubated with thrombin (2 U mL^{-1}, Sigma) for 30 min at 37 °C and stored at −80 °C in small aliquots until further use.

Synthesis of NorHA: Norbornene-modified hyaluronic acid (NorHA) was synthesized as previously reported.[48] Briefly, hyaluronic acid was converted to a tetrabutylammonium salt (HA-TBA) to make it soluble in dimethyl sulfoxide (DMSO). First, the hyaluronic sodium salt was converted to its acid form using a proton exchange resin (Dowex 50 W). After filtration, the HA was titrated to a pH of 7.03 with TBA-OH. The coupling of 5-norbornene-2-carboxylic acid to HA-TBA, was performed in DMSO, using di-tertbutyl dicarbonate (Boc2O) as a coupling agent and 4-methylaminepyridine (DMAP) as a catalyst. The reaction proceeded at 45 °C under N_2 atmosphere. The reaction was quenched after 20 h. The polymer was purified by precipitation in cold acetone and dialysis. NorHA modification was confirmed and quantified via 1H NMR spectroscopy.

Synthesis of GelMA: Methacrylate functionalized gelatin (GelMA) was synthesized according to a previously published protocol.[49] Briefly, gelatin (Type A, bloom 300, G1890-500G, Sigma–Aldrich) was dissolved in heated deionized water at 50 °C. Methacrylic anhydride (276 685, Sigma–Aldrich) was added to the mixture and stirred for 90 min. Unreacted methacrylic anhydride was removed by centrifugation. The supernatant was dialyzed and lyophilized to obtain GelMA powder. The powder was reconstituted in PBS to obtain a final stock concentration of 15 wt% GelMA, which was stored at 4 °C until further use.

Microfluidic Device Fabrication: The microfluidic devices for microgel fabrication and confinement were designed in AutoCAD (Autodesk). Master molds were fabricated by spin-coating (WS-650-23B, Laurell) an SU-8 photoresist (GM1070) onto plasma cleaned silicon wafers (Si-Wafer, Siegert Wafer). The coated layer was baked at 65 and 95 °C and patterned using the masks (high resolution film mask, Microlitho) containing device designs by alignment onto the coated silicon wafers followed by post-baking and photoresist development. The resulting wafer was post-baked at 200 °C for 10 min. Patterned wafers were treated with chlorotrimethyl silane vapor before polydimethylsiloxane (PDMS) molding. Microfluidic devices were fabricated using standard soft-lithographic techniques. A mixture of PDMS monomer and curing agent (Elastosil) at a 9:1 ratio was poured over a silicon wafer mold and peeled off after polymerization at 70 °C for 30 min. Inlets and outlets were punched using a hole puncher (20G Catheter Punch; Schmidt Press), and the PDMS substrate was bonded to a glass slide (Menzel-Glaser, Germany) in the case of droplet generation devices or a cover slip for culture devices (25 mm diameter, #1.5 thickness; Epredia) after oxygen plasma treatment (EMITECH K1000X, Quorum Technologies) of both surfaces for 60 s. Bonded devices were left on a 120 °C hot plate for 2 h to allow complete bonding.

PEGNB Microgel Fabrication: Defined microgel building blocks were fabricated via microfluidic templating of water-in-oil emulsions as previously described.[38] A Cetoni neMESYS syringe pump with a Cetoni base 120 power adapter were used as displacement syringe pumps for the aqueous and oil phases. A Nikon Eclipse Ts2 inverted microscope paired with uEye Cockpit by iDS7 was used for high-speed imaging of the microfluidic flow. Briefly, hydrogel precursor and hydrofluoro ether oil with surfactant (Droplet Generation Oil for probes, Biorad Laboratories Inc.) solutions were loaded into gastight syringes and connected to the inlets of the microfluidic device via Tygon tubing (Cole Palmer GmbH). To form droplets, an aqueous solution containing 8-arm PEGNB macromer, dithiothreitol (DTT), a cell adhesion sequence CRGDS (Genscript) and photoinitiator lithium phenyl-2,4,6-trimethylbenzoylphosphinate (LAP) was injected into the microfluidic device and pinched off by the oil phase at volumetric flow rates of 20 and 8 uL min^{-1} for the oil and aqueous phase respectively. The generated droplets were collected in a collection vial containing light mineral oil to prevent evaporation of the volatile droplet oil phase. After collection, droplets containing eight-arm star PEG macromers end-functionalized with norbornene groups (PEGNB) were cross-linked with DTT by exposure to UV light for 60 s (λ = 365 nm, I = 15 mW cm^{-2}; M365L3-C1, ThorLabs). After cross-linking, collected microgels were centrifuged at 14100 x g for 5 min, to separate the microgels from mineral oil and droplet oil. Microgels were then suspended in PBS containing 1% Penicillin-Streptomycin (PenStrep) followed by repeated centrifugation and discarding of supernatant to ensure complete removal of the oil phase. Washed microgels were stored in PBS containing 1% PenStrep at 4 °C until further use.

Rheological Characterization of PEGNB Networks: Rheometric characterization was performed using a strain-controlled shear rheometer (MCR 502; Anton-Paar; Zofingen, Switzerland) equipped with a Peltier stage to control temperature (T = 25 °C). All data were collected using a sandblasted upper geometry with an 8 mm diameter (PP08/S sandblasted) by Anton Paar. A moist KIMTECH wipe was placed in the measurement chamber to prevent the samples from drying out. Motor adjustments were performed prior to each experiment. Bulk hydrogels were prepared by cross-linking the pre-gel solution in between the two plates upon UV light exposure for 60 s (λ = 365 nm, I = 15 mW cm^{-2}; M365L3-C1, Thorlabs). Gelation time and storage (G′) and loss moduli (G″) were probed via oscillatory strain tests over time at γ = 0.1% strain amplitude and an angular frequency of ω = 1 rad s^{-1} that lie in the LVE region. Granular hydrogel samples were loaded by placing them directly on the Peltier plate and lowering the geometry to the desired gap. Between each measurement, time sweeps (TS) were performed at 25 °C to equilibrate the material response (γ = 0.1%; ω = 1 rad s^{-1}). Strain sweep (SS) experiments were performed at ω = 1 or 10 rad s^{-1} for γ = 0.001–1000%. Frequency sweep (FS) experiments were performed at γ = 0.1% (within the linear viscoelastic regime as determined from strain sweep experiments) for ω = 100–0.01 rad s^{-1}.

NorHA Microgel Fabrication through Fragmentation: Fragmented microgels were prepared by extrusion fragmentation, as previously reported.[21] Briefly, the polymer precursor solution was prepared by dissolving NorHA (4 wt%), DTT (0.08 wt%), and LAP photoinitiator (0.1 wt%) in PBS 1x. RGD (1 mM, Sequence: GCGYGRGDSPG) was added to the formulation to enhance cell attachment. High molecular weight FITC-Dextran

© 2024 The Authors. Advanced Functional Materials published by Wiley-VCH GmbH

16163028, 0, Downloaded from https://onlinelibrary.wiley.com/doi/10.1002/adfm.202310507 by ETH Zurich, Wiley Online Library on [21/05/2024]. See the Terms and Conditions (https://onlinelibrary.wiley.com/terms-and-conditions) on Wiley Online Library for rules of use; OA articles are governed by the applicable Creative Commons License

(2 MDa, 0.2 wt%) was added to the solution to visualize microgels using a fluorescent microscope. One milliliter of the precursor solution was loaded into a 3 mL syringe and cured using an ultraviolet lamp (Omnicure, 200 W Mercury Lamp – 320 – 390 nm optical filter, $I = 10$ mW cm^{-2}) for 10 min. After curing, 1 mL of PBS was added to the syringe, and the polymer was extruded through the syringe without any needle. The fragmented microgels were loaded into another 3 mL syringe and subsequently extruded using 18G, 21G, 25G, 27G, and 30G needles. The fragmented microgels were passed through the 30G needle four times and then collected between 40–200 µm filters. Microgels were suspended in PBS followed by repeated centrifugation and discarding of supernatant to ensure removal of unreacted species. The washed microgels were stored in PBS until further use. Particle size was quantified by analyzing fluorescent microgel images using ImageJ.

GelMA Microgel Fabrication through Batch Emulsification: Batch emulsification of GelMA was based on a method previously described for hyaluronic-based materials.[50] Briefly, a 10 wt% GelMA precursor solution was prepared by mixing 66.6 µL of 15 wt% GelMA stock solution with 23.4 µL PBS and 10 µL LAP. A 25 mL round-bottom flask containing 3 mL light mineral oil with 60 µL Span 80 and a magnetic stir bar was placed on a stirring plate set to 250 rpm. Next, while stirring, 100 µL of GelMA precursor solution was added dropwise and left to stir for 1 min, before UV-induced cross-linking was performed at $\lambda = 405$ nm for 3 min. After cross-linking, collected microgels were centrifuged at 14100 x g for 5 min and the mineral oil was discarded. Next, microgels were washed 2x with PBS and 2x with 0.025% Tween20 in PBS, centrifuging and discarding the supernatant at each step. Washed microgels were stored in PBS at 4 °C until further use.

Cell Culture: Human bone marrow-derived mesenchymal stem/stromal cells (hBM-MSCs, expressing CD29, CD44, CD73, CD90, CD105 and lacking CD34 and CD45, as characterized by flow cytometry) were isolated as previously described from bone marrow aspirates of healthy donors obtained during hip surgeries at Universitätsspital Basel after informed consent and in accordance with the local ethical committee (University Hospital Basel; Prof. Kummer; approval date 26/03/2007 Ref. Number 78/07).[51] Cells were expanded and maintained in MEM alpha (Gibco) supplemented with 10% FBS (Gibco), 1% PenStrep, and basic fibroblast growth factor (FGF-2; Peprotech) at a concentration of 5 ng mL^{-1} (hBM-MSC culture medium). They were then detached using 0.05% Trypsin-EDTA (Gibco) at ≈80% confluence and sub-cultured at ratios varying from 1:2 to 1:6. Cells were used between passages 5 and 9. All cultures were grown at 37 °C in a humidified atmosphere at 5% CO_2.

Chip Seeding with Single Cell Suspensions: Microfluidic chips were immobilized by capillary forces in a 6-well plate (TPP) by adding 1 µL sterile PBS into the well and adding the chip with the coverslip facing down onto the PBS. In addition, 2 mL PBS was added to both inter-well spaces of the well plate resulting in a humidified chamber to reduce medium evaporation during culture. For experiments starting with single-cell suspensions, a master mix consisting of, 4.4 µL of packed microgels and 37.5 µL methylcellulose (0.5%) were combined with 8.8 µL hBM-MSCs at a concentration of 3×10^7 cells mL^{-1} in basal medium, resulting in a final cell density of 5.2×10^6 cells mL^{-1} (volumes cautiously calculated for one chip). Next, 40 µL of master mix was aspirated with an air-displacement pipette and the confinement chamber of a PDMS chip filled until microgels reached the inlet. The remaining master mix was then added back to the original stock mix for reuse. Subsequently, the inlet was plugged with tungsten wire (ADVENT Research Material Ltd.). Ten minutes after seeding, 100 µL basal medium was injected into both lateral media channels. Samples were then incubated at 37 °C and 5% CO_2 for ≈2 h. Unless stated otherwise, the medium was changed to hBM-MSC culture medium and then chips were cultured again at 37 °C and 5% CO_2.

Spheroid Formation: AggreWell400 plates (STEMCELL Technologies) consisting of a high-density array of 1200 pyramid-shaped microwells were used to produce large numbers of spheroids of reproducible size. First, the wells to be used were pre-treated with an anti-adherence rinsing solution (STEMCELL Technologies), as described in the manufacturer's protocol. Next, the wells were rinsed with MEM-α supplemented with 1% PenStrep and 10% FBS (basal medium). Subsequently, 1 mL of a suspension of hBM-MSCs at 2.4×10^5 mL^{-1} in basal medium was added and the plate was centrifuged, resulting in the clustering of 200 cells at the bottom of each microwell. The plates were then incubated at 37 °C with 5% CO_2 for 48 h before spheroids were harvested by pipetting-based dispersion. To study spheroid outgrowth and cell infiltration, 5 µL of packed microgels, 25 µL of methylcellulose (0.5%) and 25 µL spheroid suspension (2000 spheroids mL^{-1} in basal medium) were combined per chip. Brightfield images of spheroids formed in the plate and a size distribution characterization are provided in Figure S1 (Supporting Information).

Seeding of Double-Chamber Devices for Infiltration Studies: Devices were placed into 6-well plates as described above. For the tissue-mimic, stoichiometrically balanced solutions of TG-PEG precursors 8-arm-PEG-Gln and 8-arm-PEG-MMP sensitive were prepared in Tris buffer (50 mM, pH 7.6; AppliChem) and calcium chloride ($CaCl_2$, 50 mM; Sigma). To foster cell adhesion, Lys-RGD peptide (Ac-FKGG-RGDSPG-NH2; 50 µM, Bachem) was added to the precursor solution. PEG precursor solutions were prepared at 1.7 wt%. Furthermore, 500 µg mL^{-1} bovine collagen I (Advanced Biomatrix) was added to confer additional tissue-mimicking properties. hBM-MSCs were encapsulated at 10^7 cells mL^{-1} before the cross-linking enzyme FXIIIa (10 U mL^{-1}) was added. The solution was briefly vortexed and immediately injected into the tissue chamber (2 µL per device) thanks to the capillary forces between the solution and the channel pillars.[52,53] Cross-linking was allowed to proceed for 5 min before 100 µL basal medium was added to all channels and the device was placed at 37 °C for 30 min before continuing. Next, microgel suspensions were prepared as described above, however, no cells were added. Excess medium was aspirated around the device inlets and the suspension was injected until the confinement chamber was filled and plugged, as described above. Per media channel, 100 µL of culture medium containing 0, 25, or 100 ng mL^{-1} PDGF-BB (Peprotech) was added.

Fixation and Staining: For live labeling of nuclei, cells were incubated with 8 µM Hoechst 33 342 (Thermo Fisher) in PBS for 10 min at RT before thorough washing through two rounds of centrifugation at 400 x g, followed by supernatant aspiration and resuspension in fresh PBS. For extracellular matrix staining, the primary antibody [fibronectin antibody (IST-9), sc59826, Santa Cruz, used at 1:300; anti-collagen I antibody, ab260043, Abcam, used at 1:50] was added to 100 µL of culture medium during the last overnight period of culture. At the end of culture, samples were washed with PBS (Gibco) and fixed in 4% paraformaldehyde (PFA) (Artechemis) at RT for 30 min and stored at 4 °C. Samples were subsequently incubated in a permeabilizing and blocking solution containing 1% BSA (bovine serum albumin fraction V, AppliChem) and 0.3% Triton X-100 (Sigma) in PBS. Next, samples were incubated with a secondary staining solution consisting of 1% BSA, 0.1% Triton X-100, 1:4000 rhodamine-phalloidin (Invitrogen, R415), 1 µg mL^{-1} 4′,6-diamidino-2-phenylindole (DAPI; Sigma) and secondary antibodies at 1:200 (goat-anti-mouse-AlexaFluor488, ab150113, Abcam; goat-anti-rabbit-AlexaFluor488 ab150077, Abcam; goat-anti-mouse-DyLight649, 405 312, Biolegend; donkey-anti-rabbit-DyLight649, 406 406 Biolegend). Incubation with secondary staining solution was carried out overnight at 4 °C before thoroughly washing the plates with PBS. For Ki-67 and YAP staining, samples were permeabilized as described above before primary antibodies (Ki-67 antibody, AB9260, Milipore, used at 1:200; YAP antibody, sc101199, Santa Cruz, used at 1:100) were incubated overnight at 4 °C. Secondary staining was performed as described for ECM staining after thorough washing of the samples.

Image Acquisition and Processing: During culture, samples were monitored using a Leica DMI6000B inverted epifluorescence microscope. The same microscope was used to acquire time-lapse videos. Confocal fluorescence images were acquired on a Leica Stellaris 5 confocal laser scanning microscope (CLSM). Properties of confocal stacks acquired are indicated in the figure captions of the respective figures and in the specific methods. Image processing was done in Fiji unless stated otherwise in specific methods.[54]

Quantification of Nuclei, F-actin- and ECM-Positive Areas: Stained samples were imaged using CLSM. Quantification of nuclei was done using a particle analyzer on Otsu-thresholded images, where binary images were additionally processed with watershed to separate single nuclei. Resulting

© 2024 The Authors. Advanced Functional Materials published by Wiley-VCH GmbH

16163028, 0, Downloaded from https://onlinelibrary.wiley.com/doi/10.1002/adfm.202310507 by ETH Zurich, Wiley Online Library on [21/05/2024]. See the Terms and Conditions (https://onlinelibrary.wiley.com/terms-and-conditions) on Wiley Online Library for rules of use; OA articles are governed by the applicable Creative Commons License

images and counted objects were compared to original images to confirm reliable quantification and where needed, thresholds were adjusted manually. F-actin, fibronectin, and collagen I area of maximum intensity projections were created in a similar manner, but by measuring the total area of a section and not applying watershed segmentation. 3D renderings were generated in Imaris (Bitplane).

Microgel Size Distribution, Porosity, and Pore Diameter Analysis of Confined Microgel Constructs: The size distribution of microgels was examined using CLSM. FITC-dextran (500 kDa) was flushed in the confinement chamber and z-stacks of confined microgels were acquired (pixel size 0.38 µm x 0.38 µm, 80 µm stack depth, 2.41 µm step size). For each experimental condition, eight slices containing in-focus microgels were selected and analyzed with Fiji. For every image, a median filter of radius 3 was applied. Images were inverted, then manually thresholded and binarized. Subsequently, the diameters were determined using the "Analyze Particles" tool. Full stacks as described above were used for porosity and pore diameter analyses. Processing and analysis were done in Python (script available on GitHub).[55] Briefly, individual stacks were pre-processed by applying using contrast-limited adaptive histogram equalization (CLAHE), applying a Gaussian blur followed by local Otsu thresholding. For post-processing, a median filter was applied 3 times and morphological opening and closing was performed. Finally, total void space was quantified, and porosity was calculated as percentage of total volume. Pore sizes were quantified using the snow portioning algorithm and Regionprops3D for ball fitting.[56] Representative renderings of pore size analyses are shown in Figure S10 (Supporting Information).

Proliferation (Ki-67) Analysis: To determine the relative number of Ki-67-positive cells, randomly selected regions (3–5 regions per sample, 5 samples per condition) were imaged using CLSM. Maximum intensity projections of the confocal stacks (5 µm step size, 80 µm total height) were generated and saturated outliers in the Ki-67 signal were removed (radius ≤ 25 pixels, likely antibody aggregates). Ki-67 and corresponding DAPI images were overlayed and double-positive regions were counted. Nuclei were counted as described above and the percentage of Ki-67-positive nuclei was determined for every region before averaging over the respective sample.

Yes-Associated Protein (YAP) Analysis: To determine YAP activity, randomly selected regions (3–5 regions per sample, 5 samples per condition) were imaged using CLSM, generating 80 µm stacks with a step size of 5 µm. Processing and analysis were carried out in python (script available on GitHub).[57] In brief, DAPI and F-actin signals were Otsu-thresholded and a median filter was applied thrice to generate masks for YAP intensity analysis. The average YAP signal intensity on nuclear areas was divided by the average intensity on cytosolic areas (given by F-actin) for each slice of the stacks.

Statistical Analysis: Statistical analysis was performed using GraphPad Prism (version 8.0.0). For data with a Gaussian distribution (as determined by Shapiro-Wilk test) and three conditions, statistical significance was determined by one way ANOVA and Holm-Šídák correction for multiple comparisons, with alpha = 0.05. For comparisons between two conditions, unpaired, two-tailed *t*-tests were performed. For data without a Gaussian distribution, Kruskal–Wallis with Dunn's tests (three conditions) or Mann–Whitney tests (two conditions) were performed. Respective tests performed are indicated in figure captions.

Supporting Information

Supporting Information is available from the Wiley Online Library or from the author.

Acknowledgements

L.A.K., D.B.E., and S.P. contributed equally to this work. L.A.K., D.B.E., S.P., M.W.T., and M.E. conceived the research. L.A.K., D.B.E., M.W.T., and M.E. wrote the manuscript. L.A.K., D.B.E., and S.P. designed and performed experiments and analyzed data. L.O.M. performed image-based analysis of microgel constructs and YAP localization. L.O.M, O.B., and S.Y.L.C. assisted with single-compartment experiments. G.J.R.R. and J.A.B. synthesized and provided NorHA microgels. The microfabrication was supported by A.J.dM. All authors gave feedback on the manuscript. The authors would like to thank Dr. Dhananjay Deshmukh for providing GelMA polymer and Thomas Moragues and Dr. Simon Berger for assistance with microfabrication. Confocal imaging was performed with equipment maintained by the Center for Microscopy and Image Analysis, University of Zurich. This work was supported by the Swiss National Science Foundation (SNSF) grant Nr. 205321-204318, Helmut Horten Stiftung, and the Open ETH project SKINTEGRITY.CH.

Conflict of Interest

The authors declare no conflict of interest.

Data Availability Statement

The data that support the findings of this study are available from the corresponding author upon reasonable request.

Keywords

biomaterial, cell-material interactions, granular hydrogel, microfluidics, microgels, platforms, porosity, regeneration

Received: September 1, 2023
Revised: February 26, 2024
Published online:

[1] D. R. Griffin, M. M. Archang, C.-H. Kuan, W. M. Weaver, J. S. Weinstein, A. C. Feng, A. Ruccia, E. Sideris, V. Ragkousis, J. Koh, M. V. Plikus, D. Di Carlo, T. Segura, P. O. Scumpia, *Nat. Mater.* **2021**, *20*, 560.
[2] E. M. Sussman, M. C. Halpin, J. Muster, R. T. Moon, B. D. Ratner, *Ann. Biomed. Eng.* **2014**, *42*, 1508.
[3] S. Wang, L. Li, D. Su, K. Robin, K. A. Brown, *ACS Appl. Mater. Interfaces* **2018**, *10*, 34604.
[4] N. Broguiere, A. Husch, G. Palazzolo, F. Bradke, S. Madduri, M. Zenobi-Wong, *Biomaterials* **2019**, *200*, 56.
[5] S. I. Somo, B. Akar, E. S. Bayrak, J. C. Larson, A. A. Appel, H. Mehdizadeh, A. Cinar, E. M. Brey, *Tissue Eng., Part C* **2015**, *21*, 773.
[6] P. B. Welzel, M. Grimmer, C. Renneberg, L. Naujox, S. Zschoche, U. Freudenberg, C. Werner, *Biomacromolecules* **2012**, *13*, 2349.
[7] D. R. Griffin, W. M. Weaver, P. O. Scumpia, D. Di Carlo, T. Segura, *Nat. Mater.* **2015**, *14*, 737.
[8] L. R. Nih, E. Sideris, S. T. Carmichael, T. Segura, *Adv. Mater.* **2017**, *29*, 1606471.
[9] T. H. Qazi, J. A. Burdick, *Biomater Biosyst* **2021**, *1*, 100008.
[10] A. Puiggalí-Jou, M. Asadikorayem, K. Maniura-Weber, M. Zenobi-Wong, *Acta Biomater.* **2023**, *166*, 69.
[11] M. M. Coronel, K. E. Martin, M. D. Hunckler, P. Kalelkar, R. M. Shah, A. J. García, *Small* **2022**, *18*, e2106896.
[12] C. B. Highley, K. H. Song, A. C. Daly, J. A. Burdick, *Adv. Sci.* **2019**, *6*, 1801076.
[13] S. Xin, K. A. Deo, J. Dai, N. K. R. Pandian, D. Chimene, R. M. Moebius, A. Jain, A. Han, A. K. Gaharwar, D. L. Alge, *Sci. Adv.* **2021**, *7*, eabk3087.
[14] C. S. O'Bryan, C. P. Kabb, B. S. Sumerlin, T. E. Angelini, *ACS Appl. Bio Mater.* **2019**, *2*, 1509.
[15] J. M. de Rutte, J. Koh, D. Di Carlo, *Adv. Funct. Mater.* **2019**, *29*, 1900071.

© 2024 The Authors. Advanced Functional Materials published by Wiley-VCH GmbH

16163028, 0, Downloaded from https://onlinelibrary.wiley.com/doi/10.1002/adfm.202310507 by ETH Zurich, Wiley Online Library on [21/05/2024]. See the Terms and Conditions (https://onlinelibrary.wiley.com/terms-and-conditions) on Wiley Online Library for rules of use; OA articles are governed by the applicable Creative Commons License

[16] P. S. Lienemann, T. Rossow, A. S. Mao, Q. Vallmajo-Martin, M. Ehrbar, D. J. Mooney, *Lab Chip* **2017**, *17*, 727.
[17] W. J. Jeong, J. Y. Kim, J. Choo, E. K. Lee, C. S. Han, D. J. Beebe, G. H. Seong, S. H. Lee, *Langmuir* **2005**, *21*, 3738.
[18] D. L. Braunmiller, S. Babu, D. B. Gehlen, M. Seuß, T. Haraszti, A. Falkenstein, J. Eigen, L. De Laporte, J. J. Crassous, *Adv. Funct. Mater.* **2022**, *32*, 2202430.
[19] C. W. Visser, T. Kamperman, L. P. Karbaat, D. Lohse, M. Karperien, *Sci. Adv.* **2018**, *4*, eaao1175.
[20] A. L. Liu, A. J. García, *Ann. Biomed. Eng.* **2016**, *44*, 1946.
[21] V. G. Muir, M. E. Prendergast, J. A. Burdick, *J. Vis. Exp.* **2022**, *183*, e63867.
[22] M. E. Helgeson, S. C. Chapin, P. S. Doyle, *Curr. Opin. Colloid Interface Sci.* **2011**, *16*, 106.
[23] A. S. Caldwell, V. V. Rao, A. C. Golden, K. S. Anseth, *Biomaterials* **2020**, *232*, 119725.
[24] T. H. Qazi, J. Wu, V. G. Muir, S. Weintraub, S. E. Gullbrand, D. Lee, D. Issadore, J. A. Burdick, *Adv. Mater.* **2022**, *34*, 2109194.
[25] S. Chung, R. Sudo, V. Vickerman, I. K. Zervantonakis, R. D. Kamm, *Ann. Biomed. Eng.* **2010**, *38*, 1164.
[26] W. J. Polacheck, M. L. Kutys, J. B. Tefft, C. S. Chen, *Nat. Protoc.* **2019**, *14*, 1425.
[27] Y. K. Park, T.-Y. Tu, S. H. Lim, I. J. M. Clement, S. Y. Yang, R. D. Kamm, *Cell. Mol. Bioeng.* **2014**, *7*, 15.
[28] W. J. Polacheck, R. Li, S. G. M. Uzel, R. D. Kamm, *Lab Chip* **2013**, *13*, 2252.
[29] Y. Shin, S. Han, J. S. Jeon, K. Yamamoto, I. K. Zervantonakis, R. Sudo, R. D. Kamm, S. Chung, *Nat. Protoc.* **2012**, *7*, 1247.
[30] V. Vickerman, R. D. Kamm, *Integr. Biol.* **2012**, *4*, 863.
[31] I. K. Zervantonakis, S. K. Hughes-Alford, J. L. Charest, J. S. Condeelis, F. B. Gertler, R. D. Kamm, *Proc Natl Acad Sci U S A* **2012**, *109*, 13515.
[32] A. Pathak, S. Kumar, *Proc Natl Acad Sci U S A* **2012**, *109*, 10334.
[33] D. M. Headen, J. R. García, A. J. García, *Microsyst. Nanoeng.* **2018**, *4*, 17076.
[34] L. Riley, G. Wei, Y. Bao, P. Cheng, K. L. Wilson, Y. Liu, Y. Gong, T. Segura, *Small* **2023**, *19*, e2303466.
[35] E. Sideris, D. R. Griffin, Y. Ding, S. Li, W. M. Weaver, D. Di Carlo, T. Hsiai, T. Segura, *ACS Biomater. Sci. Eng.* **2016**, *2*, 2034.
[36] S. Xin, J. Dai, C. A. Gregory, A. Han, D. L. Alge, *Adv Funct Mater* **2020**, *30*, 1907102.
[37] N. J. Darling, E. Sideris, N. Hamada, S. T. Carmichael, T. Segura, *Adv. Sci.* **2018**, *5*, 1801046.
[38] D. B. Emiroglu, A. Bekcic, D. Dranseikiene, X. Zhang, T. Zambelli, A. J. deMello, M. W. Tibbitt, *Sci. Adv.* **2022**, *8*, eadd8570.
[39] J. Patten, K. Wang, *Adv. Drug Delivery Rev.* **2021**, *170*, 353.
[40] H. Kim, S. G. Kumbar, S. P. Nukavarapu, *Curr Opin Biomed Eng* **2021**, *17*, 1.
[41] P. S. Lienemann, Y. R. Devaud, R. Reuten, B. R. Simona, M. Karlsson, W. Weber, M. Koch, M. P. Lutolf, V. Milleret, M. Ehrbar, *Integr. Biol.* **2015**, *7*, 101.
[42] N. Zoratto, D. Di Lisa, J. de Rutte, M. N. Sakib, A. R. Alves E Silva, A. Tamayol, D. Di Carlo, A. Khademhosseini, A. Sheikhi, *Bioeng. Transl. Med.* **2020**, *5*, e10180.
[43] A. R. Armiento, L. P. Hatt, G. Sanchez Rosenberg, K. Thompson, M. J. Stoddart, *Adv Funct Mater* **2020**, *30*, 1909874.
[44] M. Ehrbar, A. Sala, P. Lienemann, A. Ranga, K. Mosiewicz, A. Bittermann, S. C. Rizzi, F. E. Weber, M. P. Lutolf, *Biophys. J.* **2011**, *100*, 284.
[45] O. Y. Dudaryeva, A. Bucciarelli, G. Bovone, F. Huwyler, S. Jaydev, N. Broguiere, M. al-Bayati, M. Lütolf, M. W. Tibbitt, *Adv. Funct. Mater.* **2021**, *31*, 2104098.
[46] M. Ehrbar, S. C. Rizzi, R. G. Schoenmakers, B. S. Miguel, J. A. Hubbell, F. E. Weber, M. P. Lutolf, *Biomacromolecules* **2007**, *8*, 3000.
[47] M. Ehrbar, S. C. Rizzi, R. Hlushchuk, V. Djonov, A. H. Zisch, J. A. Hubbell, F. E. Weber, M. P. Lutolf, *Biomaterials* **2007**, *28*, 3856.
[48] W. M. Gramlich, I. L. Kim, J. A. Burdick, *Biomaterials* **2013**, *34*, 9803.
[49] D. Loessner, C. Meinert, E. Kaemmerer, L. C. Martine, K. Yue, P. A. Levett, T. J. Klein, F. P. W. Melchels, A. Khademhosseini, D. W. Hutmacher, *Nat. Protoc.* **2016**, *11*, 727.
[50] V. G. Muir, T. H. Qazi, J. Shan, J. Groll, J. A. Burdick, *ACS Biomater. Sci. Eng.* **2021**, *7*, 4269.
[51] A. Papadimitropoulos, E. Piccinini, S. Brachat, A. Braccini, D. Wendt, A. Barbero, C. Jacobi, I. Martin, *PLoS One* **2014**, *9*, e102359.
[52] M. B. Chen, J. A. Whisler, J. Fröse, C. Yu, Y. Shin, R. D. Kamm, *Nat. Protoc.* **2017**, *12*, 865.
[53] M. Campisi, Y. Shin, T. Osaki, C. Hajal, V. Chiono, R. D. Kamm, *Biomaterials* **2018**, *180*, 117.
[54] J. Schindelin, I. Arganda-Carreras, E. Frise, V. Kaynig, M. Longair, T. Pietzsch, S. Preibisch, C. Rueden, S. Saalfeld, B. Schmid, J. Y. Tinevez, D. J. White, V. Hartenstein, K. Eliceiri, P. Tomancak, A. Cardona, *Nat. Methods* **2012**, *9*, 676.
[55] Poresize-for-Microgels-Hydrogels/pore_size.py at main EarlBugsBunny/Poresize-for-Microgels-Hydrogels GitHub, https://github.com/EarlBugsBunny/Poresize-for-Microgels-Hydrogels.
[56] J. T. Gostick, *Phys Rev E* **2017**, *96*, 023307.
[57] YAP-Quantification/YAP_stuff_single_images.py at main EarlBugsBunny/YAP-Quantification GitHub, https://github.com/EarlBugsBunny/YAP-Quantification.

© 2024 The Authors. Advanced Functional Materials published by Wiley-VCH GmbH

16163028, 0, Downloaded from https://onlinelibrary.wiley.com/doi/10.1002/adfm.202310507 by ETH Zurich, Wiley Online Library on [21/05/2024]. See the Terms and Conditions (https://onlinelibrary.wiley.com/terms-and-conditions) on Wiley Online Library for rules of use; OA articles are governed by the applicable Creative Commons License